Obtaining accurate and calibrated coil models for transcranial magnetic stimulation using magnetic field measurements

A. V. Mancino[1,2,5] · F. E. Milano[1] · F. Martin Bertuzzi[3] · C. G. Yampolsky[4] · L. E. Ritacco[1,2,5] · M. R. Risk[2,5]

Abstract
Currently, simulations of the induced currents in the brain produced by transcranial magnetic stimulation (TMS) are used to elucidate the regions reached by stimuli. However, models commonly found in the literature are too general and neglect imperfections in the windings. Aiming to predict the stimulation sites in patients requires precise modeling of the electric field (E-field), and a proper calibration to adequate to the empirical data of the particular coil employed. Furthermore, most fabricators do not provide precise information about the coil geometries, and even using X-ray images may lead to subjective interpretations. We measured the three components of the vector magnetic field induced by a TMS figure-8 coil with spatial resolutions of up to 1 mm. Starting from a computerized tomography-based coil model, we applied a multivariate optimization algorithm to automatically modify the original model and obtain one that optimally fits the measurements. Differences between models were assessed in a human brain mesh using the finite-elements method showing up to 6% variations in the E-field magnitude. Our calibrated model could increase the precision of the estimated E-field induced in the brain during TMS, enhance the accuracy of delivered stimulation during functional brain mapping, and improve dosimetry for repetitive TMS.

Keywords Transcranial magnetic stimulation · Coil model · Magnetic field measurement · Electric field simulation · Calibration

1 Introduction

Transcranial magnetic stimulation (TMS) is a non-invasive method whose applications range from treatment of psychiatric, psychological, and neurological disorders [1]; determination of central motor conduction times [2]; therapeutic uses for pain relief [3], to functional brain mapping [1, 4–8]. A large time-varying current circulating a stimulation coil produces a time-varying magnetic field (B-field) that induces an electric field (E-field) in the brain, affecting neural activity. During functional brain mapping, excitations or inhibitions are delivered in neuro-navigated localized regions, and a map of eloquent regions is drawn by measuring either evoked motor potentials or the patient's performance during language tasks, which have shown good agreement with the gold-standard direct cortical stimulation [9, 10].

Depth of penetration and focality [11] are indicators employed to classify the spatial distribution of the E-field, which is the sum of a principal and a secondary component, namely the first and second terms of Eq. 1. The former is the negative time derivative of the magnetic vector potential (A-field), while the latter is the negative of the gradient of the electric potential that results from the accumulation of charges in the resistive tissue interfaces of the brain.

$$\vec{E}(\vec{r},t) = -\frac{\partial \vec{A}(\vec{r},t)}{\partial t} - \nabla\Phi(\vec{r},t) \tag{1}$$

While the primary component depends only on the coil geometry and is the main contributor of its focality when

✉ A.V. Mancino
amancino@itba.edu.ar

1 Departamento de Bioingenieria, Instituto Tecnológico de Buenos Aires, AR 1106, Buenos Aires, Argentina

2 Consejo Nacional de Investigaciones Científicas y Técnicas, Buenos Aires, Argentina

3 Servicio de Neurología, Hospital Italiano de Buenos Aires, Buenos Aires, Argentina

4 Departamento de Neurocirugía, Hospital Italiano de Buenos Aires, Buenos Aires, Argentina

5 Instituto de Medicina Traslacional e Ingeniería Biomédica, Buenos Aires, Argentina

evaluated in a volume conductor, the second component depends both on the anatomy and the primary E-field, implying that an accurate assessment of the secondary component requires equivalent accuracy on the primary [12].

A variety of coil geometry designs have been proposed. Simple round coils consist of a single spiral winding, whereas figure-8 coils concentrate higher induced E-field below the spires junction, producing a focal stimulation [11] more suitable for cortical brain mapping [13, 14]. According to [11], the most significant improvement in TMS focality has been the introduction of the standard figure-8 coil; and although several elaborate designs have been suggested, most of the existing commercial devices and research centers use the traditional figure-8 coil [15–19].

TMS simulations are primarily based on finite element, finite differences, and boundary element methods. The coil geometry, inferred from X-ray images [12, 20–22], is usually emulated using current conducting wire segments, or employing magnetic dipoles [13]. Regarding the secondary E-field, some studies model the head as a homogeneous conducting sphere [9, 11, 13, 14, 20], while others achieve more detailed models using magnetic resonance images to segment head tissues and assign conductivities [16, 19, 21–26]. Additionally, [27] studied the dynamics of neuronal responses to TMS by simulating neurons and neuronal trajectories. Therefore, determining the actual stimulated site in a human brain strongly depends on both the specific anatomy and the coil position and orientation [16, 25, 28]. For instance, peaks of gyri that run perpendicular to the induced current path in the cerebrospinal fluid exhibit an amplification effect, while regions where currents run parallel to axons are more susceptible to becoming activation zones [19]. Thus, to understand TMS effects at a neuronal level, the primary field is of paramount significance, as it describes the field's relative magnitudes in each direction. Nevertheless, models usually found in the literature omit imperfections in the windings, and might not yet be as precise as needed.

To ensure proper correspondence with reality, coil models must be contrasted against empirical data. Studies [13] and [12] measured E-field points along two orthogonal axes, with resolutions of 1.0 and 0.5 cm, correspondingly. However, they did not perform a complete mapping of the E-field. Nevertheless, according to [26], the realistic modeling of the B-field sources is a complex task due to the difficulty of knowing the exact geometry of the coil, but the E-field can be successfully estimated from a limited number of noisy B-field measurements alternately. On the contrary, [18] built a probe with two motors for azimuthal and elevation angles in a sphere representing a head model, measuring the whole E-field with 5 mm resolution and allowing to calibrate any TMS device independently from the vendor. In line with this, [29] captured 1000 points of the E-field at a depth of 1.5 cm from the coil using a robotic tool, while [17] calculated the magnetic vector potential by measuring the three components of the B-field using a computer-controlled plotter. Following a different approach, [22] measured the phase difference in magnetic resonance images acquired with and without applying TMS pulses to a phantom agar. Nonetheless, the B-field could be assessed in only one direction, and only at distances greater than 24 mm away from the stimulator.

We propose the acquisition of high-resolution three-dimensional point by point measurements of the B-field produced by a figure-8 coil, as well as a precise geometric model adjusting to this data. The obtained model should account for imperfections in the windings of the specific coil studied, delivering more precise primary E-field simulations, thus possibly leading to more accurate computer simulations of induced E-field in the brain and hence helping to determine the level of stimulation delivered.

2 Methods

The steps required to interpolate data measurements of a TMS figure-8 coil using simulated models will be described in the following sections. First, the vector B-field of the coil is measured using a three-axis Hall-effect sensor, whose analog output is converted and digitally processed. Acquired data points are spatially distributed in planes parallel to the stimulator surface at different depths, setting up the sensor on an XY table, following almost the same approach described in previous works [17]. Simulations of the B-field are obtained for the same spatial points measured using current distribution geometric models of the coil, enabling the contrast between measurements and simulations. Furthermore, an optimization algorithm is used to adjust the geometric model to the empirical data. Finally, the relevance of the performed corrections is assessed using both direct measurements of the B-field and E-field estimations in a brain model mesh using the finite element method (FEM).

2.1 TMS equipment

All experiments were conducted using a Magstim Rapid[2] TMS stimulator in repetitive mode, to drive a figure-8 Magstim Double Air Film Coil.[1] The interstimulus interval was set to 0.5 s, and the intensity was manually adjusted depending on the location of the probe.

[1] https://www.magstim.com/product/1/70~mm-double-air-film-coil

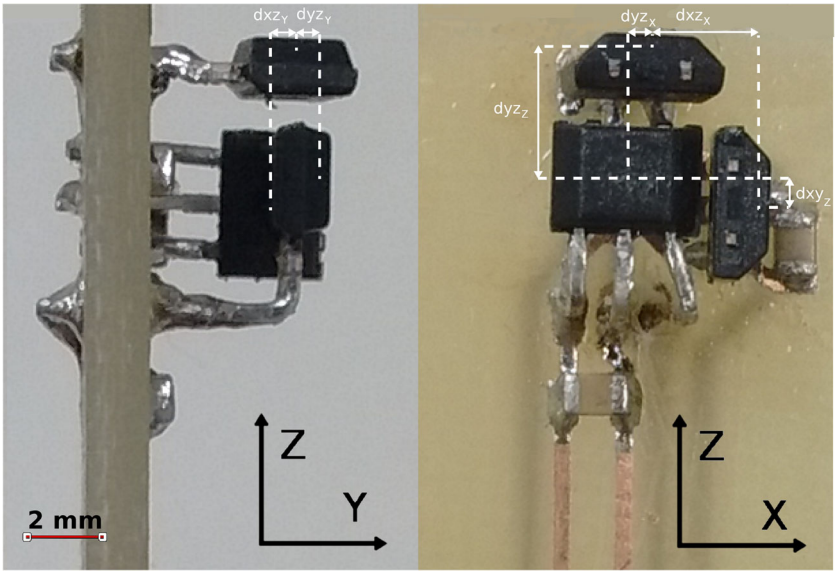

Fig. 1 Three-axis magnetic sensor built for the acquisition of the field points, using three Allegro MicroSystems A1324 flux density Hall-effect sensors

2.2 Magnetic sensor

A three-axis B-field sensor was built using three Allegro MicroSystems flux density Hall-effect sensors A1324.[2] These have 50 mV/mT resolution analog output, and fed with 5V enable − 50 to 50 mT measurements.

In order to minimize the induction of eddy currents in the three-axis sensor, the printed board plane was aligned perpendicular to the figure-8 stimulator's plane (Fig. 1). The reason for doing this is because, according to simulations, the E-field induced in the Z direction is around two orders of magnitude smaller than in the XY plane.

Since it is not possible to errorlessly align the three sensors to their corresponding Cartesian axes, a measurement correction technique was implemented, based on trigonometric principles. Given that a misalignment in one sensor away from its nominal axis leads to a decrease in the strength measurement of the former sensor and an increase in the measurement of the remaining sensors, it can be stated that:

$$\begin{aligned} b_x &= B_x \cos(\alpha_{xy}) \cos(\alpha_{xz}) + B_y \sin(\alpha_{xy}) + B_z \sin(\alpha_{xz}) \\ b_y &= B_y \cos(\alpha_{yx}) \cos(\alpha_{yz}) + B_x \sin(\alpha_{yx}) + B_z \sin(\alpha_{yz}) \\ b_z &= B_z \cos(\alpha_{zx}) \cos(\alpha_{zy}) + B_x \sin(\alpha_{zx}) + B_y \sin(\alpha_{zy}) \end{aligned} \quad (2)$$

where α_{ij} is the ith axis sensor's normal vector inclination towards the jth Cartesian nominal axis, b_i is the ith axis measurement taken, and B_i is the real magnitude of the field in such direction. Given that B_x, B_y, and B_z are unknown, corresponding approximations (B'_i) for the field magnitudes can be obtained solving for B_i:

$$\begin{bmatrix} B'_x \\ B'_y \\ B'_z \end{bmatrix} = M^{-1} \begin{bmatrix} b_x \\ b_y \\ b_z \end{bmatrix} \quad (3)$$

$$M = \begin{bmatrix} \cos\alpha_{xy} \cos\alpha_{xz} & \sin\alpha_{xy} & \sin\alpha_{xz} \\ \sin\alpha_{yx} & \cos\alpha_{yx} \cos\alpha_{yz} & \sin\alpha_{yz} \\ \sin\alpha_{zx} & \sin\alpha_{zy} & \cos\alpha_{zx} \cos\alpha_{zy} \end{bmatrix} \quad (4)$$

The sensor was calibrated using a Helmholtz coil with a theoretical uniform B-field within the radius of 3.9 mm, which is the maximum separation between sensors. The calibration consisted of estimating the aforementioned α_{ij} angles as well as on scaling the magnitudes of the three sensors for consistency.

2.3 XY table

An XY table was used to move the three-axis magnetic sensor throughout spatial planes parallel to the stimulator surface. Two step motors attached to lead screws allow the platform to move precisely $25.4/25 \cong 1.06$ mm every 200 steps (one motor revolution). The coordinate's origin was set at the center of mass of the Magstim Double Air Film Coil (Fig. 2), and the vector field points were acquired at the XY plane, parallel to the stimulator surface. Different depths (coordinate values of the Z axis) were achieved using a caliper.

A 5.29 mm spacing resolution 35 × 23 grid (805 points), covering an average area of 225.4 cm^2, was obtained for the B-field produced by the coil at depths of 6, 9, 12, and 15 mm. Two more measurements were performed covering a slightly smaller area of 196.6 cm^2, but with a 2.11 mm

[2] https://www.allegromicro.com/en/Products/Magnetic-Linear-And-Angular-Position-Sensor-ICs/Linear-Position-Sensor-ICs/A1324-5-6.aspx

Fig. 2 XY table employed to acquire high-resolution mappings of the B-field by moving the three-axis magnetic sensor through multiple spatial points located at planes parallel to the stimulator surface. The sensor starting position, the origin of coordinates, was chosen to be the center of mass of the Magstim Air Film Coil

resolution 77 × 57 grid (4389 points), at depths of 6 and 15 mm. Finally, a single 1.06 mm resolution 65 × 65 grid (4225 points) measurement was performed to assess with millimeter accuracy the location of the field peak.

In order to achieve realistic field measurements, the parallelism of the XY table and figure-8 stimulator plane must be guaranteed. The stimulator and the XY table planes were aligned perpendicular to the direction of gravity using an accelerometer. The angle between them was estimated measuring the distance between the sensor and the stimulator surface at three different points, spaced 180 mm from each other, using a caliper. Estimated angles below 0.04° were considered acceptable.

The sensor was mounted 40 cm away from the XY table, using a non-magnetizable plastic support. It was empirically observed that no disturbances in the B-field values were introduced by the XY table presence.

2.4 Digital sampling

Each sensor output, which has a bandwidth of 17 kHz reported by the manufacturer, was filtered using a fifth-order Butterworth analog filter. The resulting signal was sampled at 50 kHz using a 10-bit analog to digital converter and interpolated using a digital cubic spline filter [30]. The chosen sample rate was adequate for the measurements, as it has been previously reported that TMS B-field waveforms have an approximate bandwidth below 10 kHz [18, 23] and a fundamental frequency of 4 kHz [16]. The magnitude of each B-field component was computed as the mean value in a burst of 19 TMS pulses of the difference between the highest and lowest peaks of the sinusoidal wave obtained after interpolation. Polarity was determined by its phase.

Even though 20 TMS pulses were sampled for each point in space, we decided to average only the last 19. The first pulse in every burst was considered an outlier, given that it always had a lower magnitude compared with the remaining ones. A statistical analysis of this phenomenon is described in the "Results" section.

The obtained sensor measurements can be modeled as a composition between a deterministic signal (the B-field time signal) and samples of a stochastic process of zero mean and variance v (sensor noise). Therefore, the ensemble averaging of 19 different measurements is an unbiased predictor of the magnetic signal, with a consistent variance prediction which is reduced by a factor of 19. Throughout the whole data sampling, the power output of the stimulator was varied so as to keep the sensor outputs in high values, maintaining the signal to noise ratio always above 44 dB after averaging. Afterward, the B-field magnitudes were scaled to ensure field magnitude consistency. The scaling was performed following a map of measured intensities to account for non-linearities in the output of the stimulator. We positioned the sensor in a location with significant contribution from the three Cartesian components of the B-field and varied the output setting in the whole operation range used throughout the work, between 7 and 20% of the maximum stimulator output. We preferred this method over linear regression (R-square $>$ 0.9988), which gave estimation errors above 2% in some cases.

Measurements were assigned to their corresponding spatial localization, considering the existing distances between the sensors (Table 1). The relatively small size of these sensors, combined with the 200 steps per millimeter pace of the XY table, allows submillimetric resolution meshes of the B-field. However, for the purposes of the study, a combination of scans of 1 and 2 mm of resolution was considered to provide enough information about the B-field shape.

2.5 Coil simulations

A current distributed detailed model [12, 13, 21] of the Magstim Air Film Coil was constructed, taking as features the inner and outer radii of the windings, the position

Table 1 Relative distances between the Hall-effect sensors inside their cases, as depicted in Fig. 1. The three Cartesian components of d_{ij} vector are given, where i and j vary between x, y, and z sensors

Sensor	dxy (mm)	dxz (mm)	dyz (mm)
X	3.5	2.8	0.7
Y	0.9	0.4	0.5
Z	0.7	3.9	3.2

of their centers, the air film gap between the wires and the instrument surface, and the wire's height. The values adopted for these parameters are summarized in Table 2 and were measured from a computerized tomography (CT) performed to the coil (Fig. 3).

The B-field induced by the geometry of the coil is the curl of the magnetic vector potential (5). To numerically compute it, we used a Biot-Savart magnetostatic formulation (6). The vector $\vec{r}$ is any point in space where the field will be computed, μ_o is the permeability of free space, $\vec{dl}$ corresponds to every differential coil wire element carrying the current $I(t)$, and $|\vec{r} - \vec{r_o}|$ is the distance between the point in space $\vec{r}$ and that particular current element.

$$\vec{B} = \nabla \times \vec{A} \tag{5}$$

$$\vec{B}(\vec{r}, t) = \frac{\mu_o}{4\pi} I(t) \int \frac{d\vec{l} \times \vec{r}}{|\vec{r} - \vec{r_o}|^3} \tag{6}$$

Using MATLAB (The MathWorks, Inc., Natick, MA, USA), we approximated (6) by a summation of 38304 small line segment elements of 0.05 mm, which was adequate to converge to the numerical integral [31]. Our model considers 19 windings and even though the wire width is neglected, the model allows variations in the shape of the windings, thus contemplating alterations in the surface area of the coil, which was reported as the dominant geometrical feature in detailed models precision [22]. The wire height, on the other hand, was simulated stacking 21 filament figure-8 coils on top of each other in the Z direction.

The primary E-field from Eq. 1 was computed in a similar manner by calculating the A-field using Eq. 7, and replacing the time derivative by a scaling factor, given that it only affects the time-varying current term (8).

$$\vec{A}(\vec{r}, t) = \frac{\mu_o}{4\pi} I(t) \int \frac{d\vec{l}}{|\vec{r} - \vec{r_o}|} \tag{7}$$

$$\frac{\partial \vec{A}}{\partial t} = \frac{\partial I(t)}{\partial t} \vec{A} \tag{8}$$

2.6 Optimization algorithm

A 22-point constrained interior-point optimization method [32] was employed to find a simulation model that matches the field measurements. Departing from a detailed model based on CT images (Fig. 3), the optimization algorithm tries different combinations of parameters, generates a new model in each step, computes its induced B-field, and compares it with the empirical data. Simulated fields are adjusted taking into account the relative spatial positions of each sensor (Table 1) leading to three separate simulations for every B-field plane measured. We decided to scale all measured and simulated field components by the peak magnitude of its corresponding X component.

The metric to minimize during the optimization is the standard deviation (σ) of the difference between the normalized points of the measured and simulated fields,

Table 2 Simulation parameters used in the coil model, before and after optimization: center of each loop in X (C_X) and Y (C_Y) axes, internal and external radius as shown in Fig. 3, mean and axes-related optimization metrics (σ_i), height of the conducting wires and air film gap (offset) between the conducting coils and the bottom surface of the stimulator

Param.	Original	Optimal	Diff. (%)
C_X (mm)	− 46.0	− 45.8	− 0.4
	47.5	47.1	− 0.8
C_Y (mm)	2.9	3.3	13.8
	4.1	3.3	− 19.5
R_i^L (mm)	21.5	23.5	9.3
	23.7	25.2	6.3
R_i^R (mm)	22.6	24.7	9.3
	20.0	21.5	7.0
R_i^U (mm)	21.6	22.6	4.6
	20.5	22.2	8.3
R_i^D (mm)	21.5	23.2	7.9
	22.4	21.1	−5.8
R_o^L (mm)	45.6	47.2	3.5
	46.3	48.2	4.1
R_o^R (mm)	45.0	46.9	4.2
	44.7	46.0	2.9
R_o^U (mm)	45.7	46.6	2.0
	45.0	45.5	1.1
R_o^D (mm)	44.4	45.1	1.6
	44.9	46.8	4.2
Offset (mm)	6.0	5.9	− 1.7
Height (mm)	15.0	17.7	18.0
15 mm			
σ_x	3.1	2.5	− 18.7
σ_y	4.8	2.6	− 45.2
σ_z	7.2	2.8	− 61.7
σ_{mean}	5.0	2.6	− 47.7
6 mm			
σ_x	5.5	3.8	− 31.4
σ_y	6.6	3.3	− 49.7
σ_z	12.5	6.0	− 52.1
σ_{mean}	8.2	4.4	− 46.8

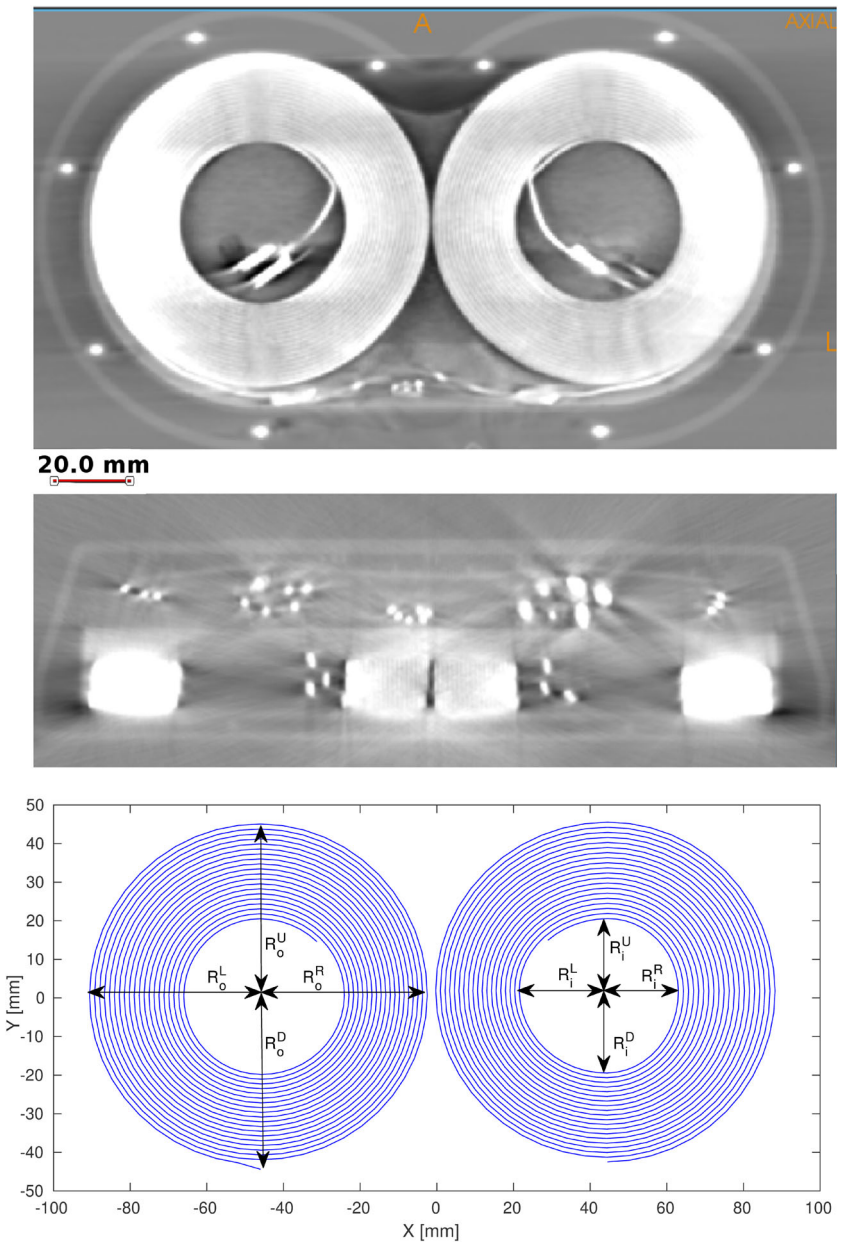

Fig. 3 Axial and coronal views of the CT image of the Magstim figure-8 Air Film Coil used to model the starting figure-8 coil geometry. Internal and external radius parameters are labeled for both loops

multiplied by 100. An index of 0.0 represents the best possible matching, while any other value (always positive) is associated with the mean difference between normalized measured and simulated fields. Given that the optimization deals with a non-convex problem, meaning that the iterative process could get stuck in local minima, we restricted the parameters to variations of up to 3 mm to encourage convergence towards a realistic model.

2.7 Comparison between measured and simulated B-fields

The percentage error between an arbitrary field $\overrightarrow{F}$ and a reference field $\overrightarrow{F_o}$ is given by Eq. 9. We compute the percentage error between the measurements and the different models by taking the module of the vector subtraction between the simulated and measured magnetic fields and dividing it by the maximum absolute value of the measured field. Since we did not measure the circulating current through the coil, we adjusted this parameter to scale the simulations and calibrate the model to the measurements. We decided to match the magnitude values in the center of the field, specifically at the peak of the X component, making the error zero at this point.

For comparisons between the simulated B-fields of two different coil geometries, we followed the same percentage error calculation of Eq. 9 but decided to directly set the same

current value in both models.

$$\text{error} = \frac{|\overrightarrow{F} - \overrightarrow{F_o}|}{\max(|\overrightarrow{F_o}|)} \times 100\% \quad (9)$$

We noticed that the center of mass of the TMS coil did not correspond exactly to the center of the B-field. Given that we seek to guarantee that the optimization metric reflects the shape inaccuracy between the simulated fields and not merely a bad rigid registration between them, before comparing the obtained solution against the original model, the latter was translated in order to align it to the measured field. While the optimal model adapts itself and autoregisters to the measurements, the location of the original design had to be determined empirically, attempting to minimize the difference against the measurements. This alignment was assisted using measurements with a spatial resolution of 1 mm, and its final form is detailed in the results.

2.8 Simulation of the E-field

The E-field induced in the vacuum is simulated for both the original and the optimal coil model, and both fields are contrasted computing the percentage deviation between them.

In order to quantify the impact of our calibration in a more realistic context, we applied the FEM to a 3D tetrahedral mesh of a healthy 28-year-old male human head so as to assess the differences in the induced TMS stimulation between the original and the optimal coil model. The mesh, consisting of 887106 elements, was partitioned in six main tissues, whose assigned conductivities were chosen from previous works [26]. These are skin (0.43 S/m), compact bone (0.009 S/m), spongy bone (0.034 S/m), cerebrospinal fluid (1.79 S/m), gray matter (0.26 S/m), and white matter (0.17 S/m). We used SCIRun 5.0 (Scientific Computing and Imaging Institute, Utah, USA) for our simulations.

The coil was positioned tangentially to the scalp at a height of 5 mm, oriented 45 degrees to the medial-sagittal plane of the subjects head, which is a common practice for the stimulation of the motor area.

2.9 Parameters sensitivity

Simulations were performed by varying one optimization parameter at the time, seeking to evaluate the sensitivity of the precision of the model concerning these alterations. We attempt as well to quantify the impact each of these variations represents relative to the total improvement achieved after the optimization. For that goal, we arranged the 22 parameters into the following six groups: Ri and Ro for the internal and external radii, Cx and Cy for the X- and Y-positions of the centers, Offset for the air film gap, and Height for the wire's height. All simulation parameters are the ones of the optimal model to which the optimization method converged, except for the ones being evaluated, which are modified by 1.0 mm in the direction towards the value of the original model.

The analysis was performed both for the B-field computed by Biot-Savart and for the E-field induced in the human brain FEM model. In the former, we measured the variation in the optimization metric, while in the latter, we measured the global maximum percentage error. We used (9), where $\overrightarrow{F}$ is the E-field resulting from the variation of each parameter, and the reference field $\overrightarrow{F_o}$ is the E-field induced by the optimal model.

2.10 Data availability

Scripts written in MATLAB to create asymmetric figure-8 models, compute its induced B-field and E-field, and for exporting them to SCIRun format are publicly available (https://github.com/amancino/TMS-coil-model.git).

3 Results

3.1 Waveform measurements

We measured a total of 5700 20 pulse bursts and compared the magnitude of each first pulse against the mean value of the remaining 19. It was determined that the first pulse of each burst has a consistent lower amplitude, 0.974 times (std = 0.01) the average of the remaining pulses.

3.2 B-field measurements

It was observed that measurements are, as expected, particularly sensitive to both the offset and the height of the coils, as previously reported in another study [12].

A particular result encountered for the Magstim Double Air Film Coil was the displacement of 3.3 mm in the positive direction of the Y-axis between the central point of stimulation and the center of mass of the coil. Therefore, further comparisons between simulations and measurements are performed after a rigid transformation correcting this displacement, as already mentioned in the "Methods" section.

Despite the fact that the three scalar components of the measured B-field are coherent with the original model simulations, significant differences between them arise. Discrepancies are observed in the lobes width, as well as in their positioning, relative magnitudes, and symmetry (Fig. 4). These asymmetries might be attributed to the inability to simulate the exact 3D geometry of the coil, contemplating its windings imperfections and all the physical phenomenons regarding the circulating current distribution.

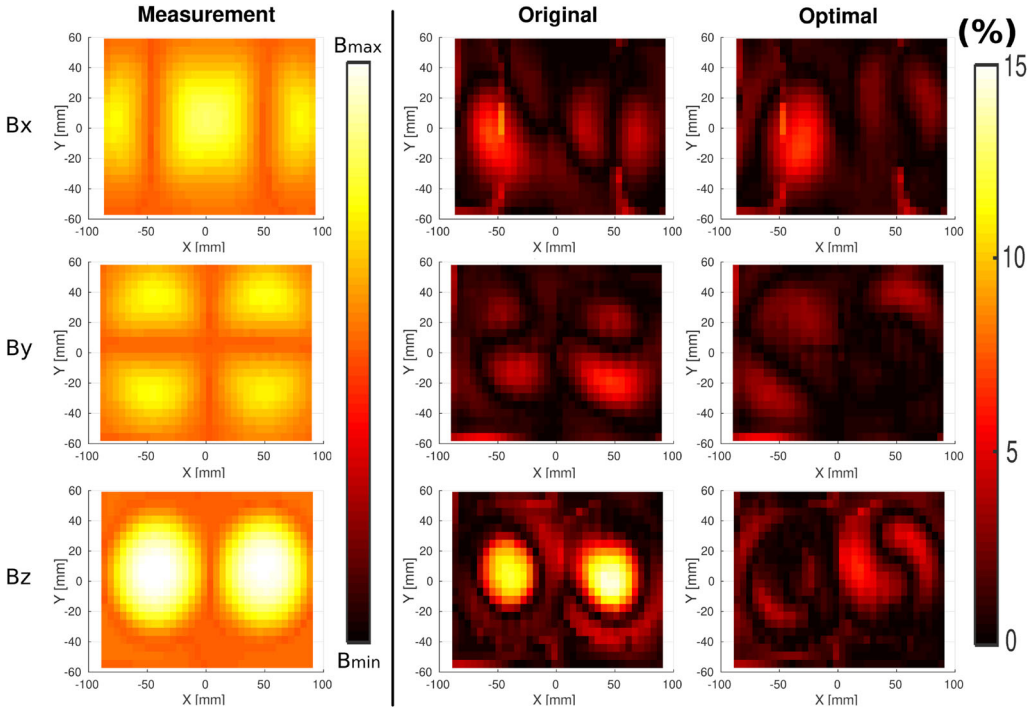

Fig. 4 The first column shows the B-field measured components at a depth of 6 mm. Rows 1–3 show each Cartesian component X, Y, Z of the vector field. The second and third columns show the percentage difference between the measurement and its corresponding simulated B-field using the original and the optimal coil geometries correspondingly. The original model centers were moved 3.3 mm in the Y-direction to minimize their difference against the measurements

Moreover, CT images might be challenging to interpret due to artifacts introduced by metal components of the coil, which lead to subjective determinations of coil parameters. It can be noticed from Fig. 3 that the relative distance between both windings is, in fact, a function of the Z coordinate. Nevertheless, most studies disregard these issues and use uncalibrated figure-8 models. Even small differences in the estimation of wires distance to the outer surface of the coil housing may result in marked changes of the absolute B-field strength at, for example, the brain surface [17].

3.3 Optimization process

The interior-point optimization process converged towards the parameters is shown in Table 2, while the obtained coil geometry for those parameters can be appreciated in Fig. 5. The optimization metric of each Cartesian component of the field, as well as its mean value for the vector field, is summarized in Table 2, for both the farthest (15 mm) and the nearest (6 mm) distances away from the stimulator surface. At greater distances, details become less relevant, and both models converge to similar B-field values, with mean standard deviation indexes between them of 1.39 for 22 mm and of 0.85 for 30 mm, for instance. This adaptation between simulations for distant points agrees with the results previously reported by other works [12, 22].

3.4 Evaluation of the obtained model

The difference between the simulations of the original against the optimal coil can be seen in the upper plot of Fig. 6, where a cut in $Y = 3.3$ mm of the B-field module is shown, for an equal circulating current, at a depth of 6 mm. The percentage difference between these simulations in the whole field with a resolution of 2 mm is shown in the contour graph of Fig. 7, both for the B-field and the E-field induced in the vacuum.

The bottom plot of Fig. 6 shows the comparison between the two models previously contrasted, but adjusting the circulating current of each of the models to match the magnitudes in the center of the field ($X = 0$ mm). The same comparison is shown for every measured point in Fig. 7, where a remarkable discrepancy between the measurements and the original simulation using the starting parameters for the coil design can be observed, with percentage differences reaching 15% in the Z component.

At 6 mm of depth, the obtained mean standard deviation of the difference between normalized B-fields was 8.2, whereas after optimization, it was lowered down to 4.4. At 15 mm of depth, the mean standard deviation is lowered from 5.0 to 2.6. Therefore, it can be stated that the obtained model converges to a solution which matches more precisely with the measurements than the X-ray images

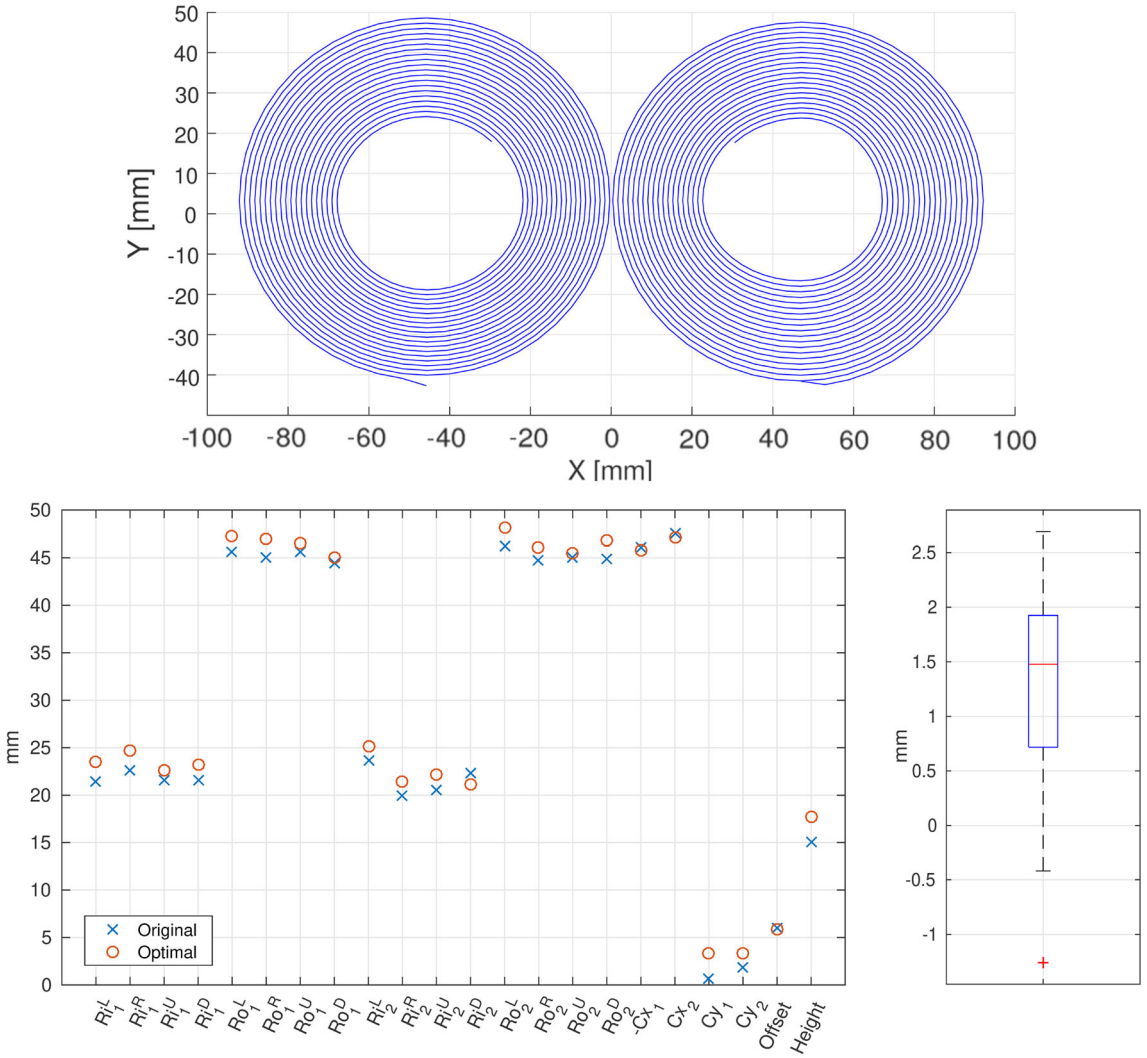

Fig. 5 Obtained coil geometry after running the optimization algorithm; and its comparison against the original one, considering the 22 parameters. The boxplot graph shows the dispersion of the distribution of the difference between optimal and original parameters, which results in a mean variation of 1.23 mm and a standard deviation of 1.01 mm

based model. At this depth, the error introduced by an inaccurate model is 6.3% in the central region for the B-field, and 3.4% in the primary E-field induced in the vacuum (Fig. 7).

Results show a tendency of the Z component of the field to have a lower amplitude than the one represented by the simulations, close to the coil. This considerably deteriorates the optimization metric for this component, as seen in Table 2; and could be explained by the proximity effect [12, 31, 33]. This phenomenon implies that in the central stimulation zone, between the two windings, the circulating currents tend to be distributed in the outermost part of each wire, virtually bringing them closer together and increasing the strength of the X component of the B-field in this region. Since all the field components were chosen to be scaled by this magnitude, an increase relative to the Z component could explain a corresponding decrease of the latter.

It is worth mentioning how the optimal Y-position of the windings' centers (C_Y), both located at 3.3 mm, corresponds with the displacement empirically found to minimize the difference between the original coil simulations and the measurements (Fig. 4). This result reinforces the assumption that the optimization algorithm converged to a valid set of parameters.

3.5 Simulated E-field in the brain

The magnitude of the simulated induced E-field in the FEM model for both the original and optimal coils is shown in Fig. 8. To illustrate the regions most prone to be stimulated, the coloring is only applied to the areas representing E-field strengths higher than 75% of the maximum peak. Figure 8 depicts the magnitude of the vector difference between the E-fields induced by the original and the optimal coils,

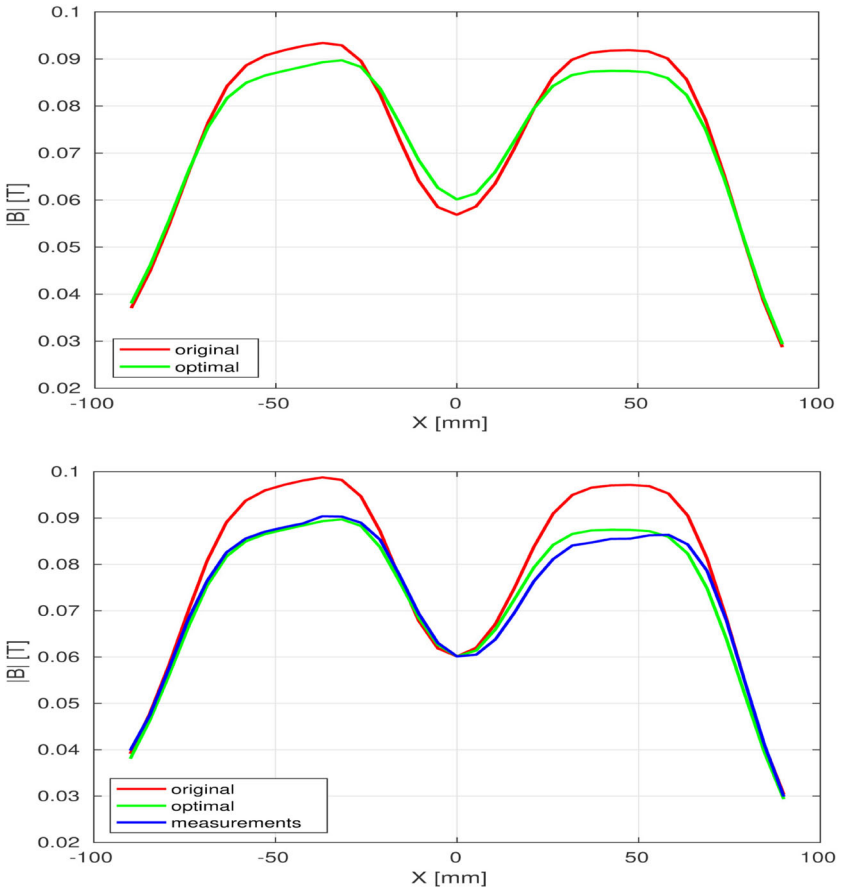

Fig. 6 Comparison between simulated field quantities acquired at a depth of 6 mm, and plotted as a function of the X coordinate, with Y fixed at 3.3 mm. Two different approaches are shown: (top) considering the same circulating current for both simulations and (bottom) adjusting the current of each model to match simulations with measurements at the center of the field

where differences reach 6% of the optimal coil induced peak value.

3.6 Parameters sensitivity

Table 3 shows the sensitivity analysis of the parameters, while the results of all simulated variations in the FEM model are shown in Fig. 3. In agreement with what was observed during the measurements, the X- and Y-positions of the centers are essential for the computation of the B-field and represent variations in the optimization metric of 20.46% and 14.36%, respectively. Their influence in the E-field is critical as well, with 52.15% and 36.82% impact, respectively. On the other hand, the external radius variation was the most relevant parameter for the E-field. Considering that a decrease of 1 mm in the external radii of both windings means a percentage reduction of the coil's area of 5.6%, while an increase of 1 mm in the internal radii results in a percentage reduction of 2.9%, it emerges that the surface of the windings is a relevant factor while modeling TMS coils, in agreement with the observations of [22].

The sensitivity impact percentages are generally higher in the E-field than in the B-field, which would seem to indicate that the former is more sensitive than the latter. Moreover, the fields are markedly sensitive to different parameters. While the air film offset has an impact of 3% in the B-field, its contribution is negligible in the E-field. Regarding the wire height, a variation of 1.0 mm practically does not alter the B-field (0.42% impact) but has a significant influence on the E-field (33.07% impact).

4 Discussion

Our results clearly demonstrate that the actual B-field induced by TMS coils present marked asymmetries compared with the original simulations, which tend to be symmetrical due to oversimplified modelings of the coil geometries. Relative differences in the B-field estimations up to 15%, as measured in this study, may lead to inaccurate simulations and unreliable stimulation site predictions. We acknowledge the fact that these errors appear close to the stimulator surface, where TMS targeting does not usually take place. Nonetheless, a precise model should adequately represent distant areas from the stimulation target as well, since activation zones in the brain are not linear mappings of the primary E-field but greatly depend on the anatomy of the patient, and even distant tissues can contribute to the

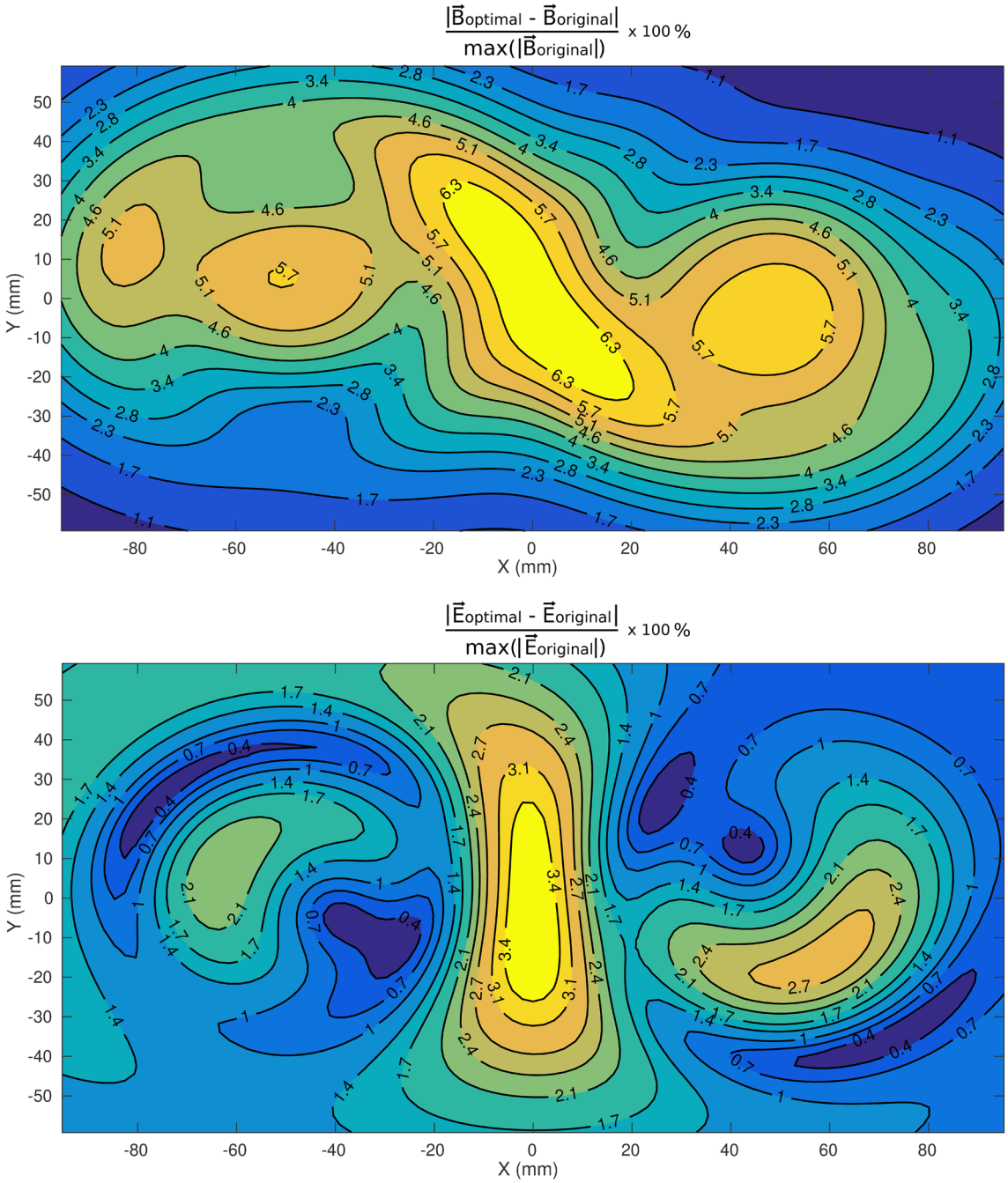

Fig. 7 Percentage difference between initial and optimal simulations of the B-field (top) and the E-field induced in the vacuum (bottom). Fields were simulated at a depth of 6 mm, considering the same circulating current in their windings, as shown in the bottom plot of Fig. 6

actual secondary field. Consequently, we believe that more precise models are needed in TMS practice, especially with the advent of improvements in the precision of numerical field simulation methods.

However, obtaining more detailed models is a complex task. Coils are not wound perfectly, and inner tension of the wires lead to asymmetric locations of the coil centers in both X- and Y-directions. The CT images acquired in this work reveal the geometric properties of the Magstim Air Film Coil, but also show that the windings present distortions in their radii, rotations, and that they are not even correctly aligned parallel to the surface of the stimulator housing. We have estimated 0.2 and 0.4 mm displacements in the position of the centers of the coils in the X-direction, and 0.4 and 0.8 mm for the Y-direction. These imperfections yield to regions where the wires are closer or further than expected and might explain the inaccuracy of our original model to match the measurements. Although the CT images were

Table 3 Parameters sensitivity analysis results for the B- and E-fields. The former is represented by the variation of the optimization metric, while for the latter measures the peak percentage difference between simulations

		C_X	C_Y	R_i	R_o	Height	Offset
B-field	$\Delta\sigma$	3.83	2.69	1.52	1.48	0.08	0.55
	Impact (%)	20.46	14.36	8.12	7.94	0.42	2.96
E-field	Error (%)	2.87	2.03	1.86	5.95	1.82	0.03
	Impact (%)	52.15	36.82	33.73	108.00	33.07	0.49

useful for counting the number of loops and for estimating the mean inner and outer radii, artifacts in the acquisition led to ambiguous parametrization of, for example, the height of the coil, whose value was indeed adjusted 2.7 mm by the optimization method.

Our results not only demonstrate that the validation of the coil model against real B-field measurements highlights flaws in the coil modeling but also that these disagreements can be minimized by adapting the model through an automatic process. We managed to design a device capable of measuring the B-field in the three Cartesian directions, at different depths; and then we managed to optimally fit a model to these measurements using a multivariate convergence algorithm. Consequently, we achieved to reduce the difference between the measurements and the simulations from 15% to around 5% (Fig. 4). Given that the problem is non-convex, the optimization algorithm might converge to a local minimum state different from the real geometric solution. Nevertheless, this work seeks an alternative parametrization that results in more reliable estimations of the B-field at depths of 6, 9, and 15 mm simultaneously, even if its final form deviates from reality.

Regarding the optimization results, the Z components of the simulated B-field showed the worst optimization metrics in Table 2 due to their tendency of having higher amplitudes than the measurements, especially when closer

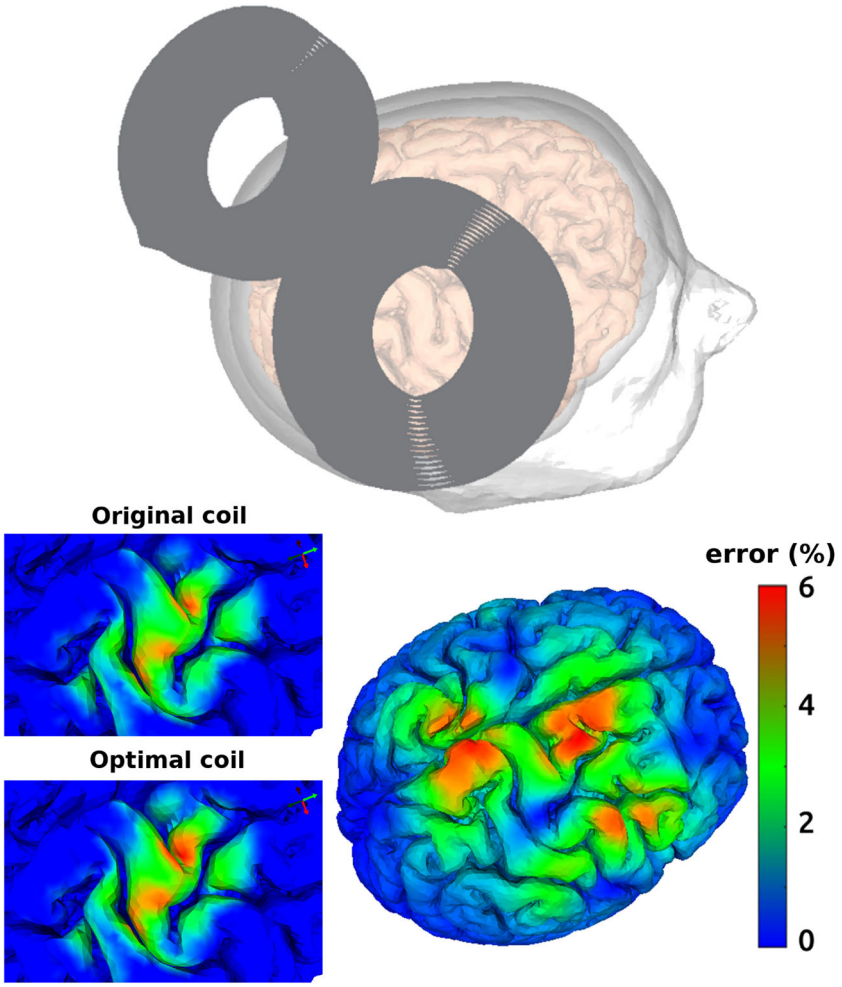

Fig. 8 Positioning of the coil in the motor area of a human head FEM model, at 45 degrees from the midline. Only areas with resulting E-field intensities above 75% of the global maximum are shown, for each one of the two models. The percentage difference between the E-field induced by the optimal model relative to the original reaches a peak difference of 6%

to the stimulator. This consistent bad performance of the Z component could be explained by the fact that its corresponding sensor was the nearest to the TMS coil during the acquisitions, namely 3.9 and 3.2 mm closer than the X and Y sensors, respectively (Table 1). However, the optimal model adapted to this scenario by proposing larger external radii (R_o^R of the left coil and R_o^L of the right coil). This managed to bring the windings closer to each other, even to the point where they partially overlapped. This physically impossible behavior might be attributed to our decision of neglecting the width of the wires and to the proximity effect, which might make the current flow in the outermost surface of the wires, and whose contribution becomes relevant at closer distances to the coil. Nevertheless, the optimized model achieved to increase the X component of the field and thus decreased the relative difference against the Z component, making the simulations converge to more suitable representations of the measurements.

We applied a Biot-Savart approximation with 21 thin wire loops consisting of 1824 line segments each, stacked onto each other for modeling with sufficient accuracy the figure-8 coil [31]. Although a magnetic dipole modeling like the one proposed by [13] would benefit from a considerably faster computation time for equivalent results [31], we consider that a deformed version of the wires' geometry allows a direct visual appreciation of the corrections applied to the model and allows clear interpretations of the intentions behind the optimization adjustments. We found this approach far more appropriate for detecting possible deformations or induced abnormalities in the model.

Using the obtained optimal coil model, we were able to calculate the vector potential, which is an input of our FEM model for the estimation of the E-field in a brain mesh. That is, we designed a method that automatically finds one valid solution for the A-field, which satisfies the condition that its curl optimally approximates the empirical measurements of the B-field, following the same approach as previous studies [17, 26]. This simulation alone can be used, as well, to estimate the main properties of the primary E-field: direction, amplitude, and focality.

One significant remark is the fact that we only measured one particular unit of the Magstim figure-8 Air Film Coil, therefore impeding us to provide a dispersion analysis of the geometric parameters. This means that the optimal parameters obtained in Table 2 may differ from coil unit to coil unit, and it may not be true that every Magstim Air Film Coil behaves in the same manner, producing specifically the identical field distribution as the one reported in this work. Nevertheless, we accomplished to introduce a calibration method that has no impediments for its application in any other coil design, and although the scope of this work was limited to figure-8 stimulators, it would only demand a change in the simulated geometric model and a new parametrization to generalize it to other types of coils. Thus, it can be used to characterize existing and new TMS coils and to provide validated geometric models for precise B-field estimations. It could be of great value a future categorization of coil prototypes based on the measurement of multiple different coils for each model, determining a tolerance in the precise values of the parameters. This could potentially lead to more standardized results while simulating a specific coil model, or at least help in determining measures of statistical dispersion of coil models for TMS users. It is noteworthy that the choice of deforming a coil geometry allows its direct application in existing TMS simulation packages, as long as they allow loading custom-designed models. We provide the web link to a repository containing all the methods developed in MATLAB for the generation of the coil geometries described in this study, which are compatible with SCIRun.

In this study, we sought to improve the model accuracy for areas closer to the stimulator. Although the stimulation targets considered in TMS practice are the brain cortex or the gray-white matter interface, tissues like the skin, bone, or even the cerebrospinal fluid contribute as well to the induced E-field in deeper regions. These components are located closer to the coil, where the precision of most models considerably worsens due to the lack of coil geometry details [12, 22]. Discrepancies between our original and optimal models translate into differences in dosage levels delivered to patients. This phenomenon is enhanced in the stimulation of animals due to their smaller heads, or in the stimulation of the spine and nerves since these are usually located nearer to the surface of the coil. We intended to provide more precision in this regard, since, to our knowledge, no previous studies have focused on obtaining good correspondence with measurements at such close distances.

Although the most notorious limitation of the present work is the decision of measuring the B-field to afterward compute the E-field, instead of directly measuring the E-field, this is the decision that enabled the use of smaller probes, and that allowed higher resolution acquisitions than the ones obtained in earlier works [12, 13, 23]. Moreover, measuring the E-field would require placing the probe in a large tank resembling a semi-infinite medium to reduce boundary effects [22, 23], or building metalic models to resemble the human head [18], hindering the experiment. During our study, the exact locations of the sensors were contemplated when contrasting the measured and simulated fields, given that the scalar field components in each direction of the vector field were compared separately during the optimization process. A considerable improvement, however, would be the use of three-axis magnetic sensors directly integrated within the same chip, greatly simplifying the measurements and avoiding to make assumptions about the deviation of the sensors and their

relative positions. Works like [26], which require direct B-field measurements, would benefit as well from these improvements.

We attempted as well to shed some light on how much error is introduced in the E-field computation due to small parameter variations. Herein, we decided to study this phenomenon in the motor cortex, which is a well-investigated region in TMS. We report, for variation of 1.16 ± 1.36 mm, up to 6% discrepancies relative to the peak magnitude in the induced E-field in the brain motor cortex. The percentage error distribution is different between B- and E-fields; and even parameters that represent a significant change in the B-field may not affect the E-field at all, or vice-versa. Our sensitivity analysis of the E-field in Fig. 9 and Table 3 agrees with the observation of [22] that the coil area is the most relevant parameter while modeling a TMS coil. The sensitivity contribution of the external radius (Ro) is approximately three times higher than the internal one (Ri), in line with the fact that the percentage change in the surface of the coil due to 1 mm variation in Ro doubles the change introduced by an equivalent variation in Ri, on the opposite direction.

Although we acquired the B-field points in uniform grids to visually appreciate the consistency in the shape of the field, measurements are not strictly subjected to this distribution. Knowing the exact location of arbitrary measured points would allow specific point simulations and a restricted application of the optimization method. In our search for greater precision, we decided to employ as many significant points as possible, attempting to avoid excessively slow optimizations. Although we obtained acquisitions at resolutions of up to 1 mm, they were only used to find the position of the center of the B-field, which resulted to be shifted 3.3 mm in the Y-direction from the center of mass of the coil. For the optimization, we used 33×25 grids of 5 mm resolution and 77×57 grids of 2 mm resolution, at parallel planes located at 6, 9, and 15 mm away from the stimulator. We sought to ensure proper modeling of the simulated B-field by matching it to the empirical data throughout the entire field distribution. Future work could evaluate the number of points and their required distribution to ensure an equivalent convergence of the optimization method using fewer acquisitions. Besides, the magnetic sensor could be mounted on an XYZ table, for automatic acquisitions at any point in space, and not only confined to XY planes. These improvements could dramatically shorten both the measurement, simulation, and optimization times. Additionally, the incorporation of a third motor for the Z direction, combined with the miniaturization of the three-axis sensor, would allow obtaining denser grids and greater volumes, in an easier alignment procedure. This arrangement, although time-consuming, could enable the direct loading of the B-field measurements into the numerical E-field calculation models.

We believe that a proper coil model calibration based on B-field measurements should rely on a wide region of the field, and not solely on the matching of values in, i.e., only the central region of it. Our calibrated model of distributed currents can increase the precision of studies that estimate the secondary E-field using the primary one, therefore promoting more realistic validations of these methods against clinical results observed in patients. Our results suggest that the calibrated model allows a more reliable interpretation of the physiological effects of TMS since it can predict more accurately the E-field induced in the brain. Herein, it can help to improve the conversion from stimulator output setting to E-field magnitudes, refining the comparison of delivered stimuli in the different regions of the brain of the same patient, or even between subjects. This

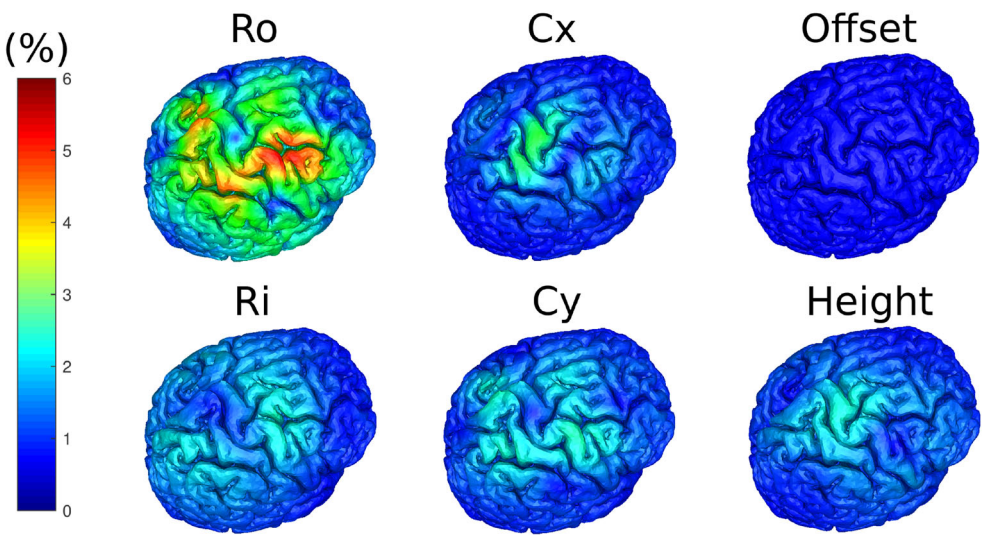

Fig. 9 Sensitivity analysis of the coil parameters evaluated for the E-field induced at the human head FEM model. Each simulation shows the percentage difference of the induced E-field of an altered version of the optimal coil, relative to the one induced by the latter. Each simulation modifies all its parameters by 1 mm in the direction towards the value of the original coil, thus showing an estimation of the percentage error introduced in the computed E-field by 1 mm variation in a parameter value

improvement can impact the use of repetitive TMS since it facilitates the monitoring of the patient's evolution, as well as the contrast between patients. Navigated functional brain mapping would also benefit from more accurate stimulation dosimetry, given that the knowledge of the stimuli strength is mandatory, and improvements in reliability could mean smaller craniotomies [5, 6] or even reduce the need of awake surgeries [4].

5 Conclusion

Modeling the coil geometry using parameters estimated from X-ray images, which are in some cases tied to subjective interpretations, might not be the most accurate approach for simulating the primary E-field. There are so many details omitted such as the distance between the two windings, the relative position of their centers, the width of the cables, the thickness of the plastic case, the offset between the coil and the housing, or even the proximity effect affecting the current distribution inside the wires; that it appears to be convenient to build a specific calibrated model for the particular coil used. In this way, if the B-field simulations optimally correlate with empirical data, then the asymmetries and imperfections of the windings will be partially compensated by the introduced asymmetries of the proposed model. More precise primary E-field simulations will imply more accurate stimulation predictions, improving the delivered stimuli dosimetry and turning TMS into a more reliable technique.

References

1. Ruohonen J, Karhu J (2010) Navigated transcranial magnetic stimulation. Neurophysiol Clin 40:7–17. https://doi.org/10.1016/j.neucli.2010.01.006
2. Udupa K, Chen R (2013) Central motor conduction time. Handb Clin Neurol 116:375–386. https://doi.org/10.1016/B978-0-444-53497-2.00031-0
3. Galhardoni R, Correia GS, Araujo H, Yeng LT, Fernandes DT, Kaziyama HH, Marcolin MA, Bouhassira D, Teixeira MJ, de Andrade DC (2015) Repetitive transcranial magnetic stimulation in chronic pain: a review of the literature. Arch Phys Med Rehabil 96:156–172. https://doi.org/10.1016/j.apmr.2014.11.010
4. Krieg SM, Sollmann N, Hauck T, Ille S, Meyer B, Ringel F (2014) Repeated mapping of cortical language sites by preoperative navigated transcranial magnetic stimulation compared to repeated intraoperative DCS mapping in awake craniotomy. BMC Neurosci 15. https://doi.org/10.1186/1471-2202-15-20
5. Sollmann N, Ille S, Hauck T, Maurer S, Negwer C, Zimmer C, Ringel F, Meyer B, Krieg SM (2015) The impact of preoperative language mapping by repetitive navigated transcranial magnetic stimulation on the clinical course of brain tumor patients. BMC Cancer 15. https://doi.org/10.1186/s12885-015-1299-5
6. Krieg SM, Sollmann N, Obermueller T, Sabih J, Bulubas L, Negwer C, Moser T, Droese D, Boeckh-Behrens T, Ringel F, Meyer B (2015) Changing the clinical course of glioma patients by preoperative motor mapping with navigated transcranial magnetic brain stimulation. BMC Cancer 15. https://doi.org/10.1186/s12885-015-1258-1
7. Ottenhausen M, Krieg SM, Meyer B, Ringel F (2015) Functional preoperative and intraoperative mapping and monitoring: increasing safety and efficacy in glioma surgery. Neurosurg Focus 38. https://doi.org/10.3171/2014.10.FOCUS14611
8. Duffau H (2011) Brain mapping - from neural basis of cognition to surgical applications. Springer, Wien. https://doi.org/10.1007/978-3-7091-0723-2
9. Picht T, Schmidt S, Brandt S, Frey D, Hannula H, Neuvonen T, Karhu J, Vajkoczy P, Suess O (2011) Preoperative functional mapping for rolandic brain tumor surgery: comparison of navigated transcranial magnetic stimulation to direct cortical stimulation. Neurosurgery 69:581–588. https://doi.org/10.1227/NEU.0b013e3182181b89
10. Tarapore P, Tate M, Findlay A, Honma S, Mizuiri D, Berger M, Nagarajan S (2012) Preoperative multimodal motor mapping: a comparison of magnetoencephalography imaging, navigated transcranial magnetic stimulation, and direct cortical stimulation. J Neurosurg 117:354–362. https://doi.org/10.3171/2012.5.JNS112124
11. Deng ZD, Lisanby SH, Peterchev AV (2013) Electric field depth–focality tradeoff in transcranial magnetic stimulation: simulation comparison of 50 coil designs. Brain Stimul 6. https://doi.org/10.1016/j.brs.2012.02.005
12. Salinas FS, Lancaster JL, Fox PT (2007) Detailed 3D models of the induced electric field of transcranial magnetic stimulation coils. Phys Med Biol 52:2879–2892. https://doi.org/10.1088/0031-9155/52/10/016
13. Thielscher A, Kammer T (2004) Electric field properties of two commercial figure-8 coils in TMS: calculation of focality and efficiency. Clin Neurophysiol 115:1697–1708. https://doi.org/10.1016/j.clinph.2004.02.019
14. Lontis ER, Voigt M, Struijk JJ (2006) Focality assessment in transcranial magnetic stimulation with double and cone coils. J Clin Neurophysiol 23:462–471. https://doi.org/10.1097/01.wnp.0000229944.63011.a1
15. Talebinejad M, Musallam S (2010) Effects of TMS coil geometry on stimulation specificity. Conf Proc IEEE Eng Med Biol Soc 1507–1510. https://doi.org/10.1109/IEMBS.2010.5626840
16. Bijsterbosch JD, Barker AT, Lee KH, Woodruff PWR (2012) Where does transcranial magnetic stimulation (TMS) stimulate? Modelling of induced field maps for some common cortical and cerebellar targets. Med Biol Eng Comput 50:671–681. https://doi.org/10.1007/s11517-012-0922-8
17. Madsen KH, Ewald L, Siebner HR, Thielscher A (2015) Transcranial magnetic stimulation: an automated procedure to obtain coil-specific models for field calculations. Brain Stimul 8:1205–1208. https://doi.org/10.1016/j.brs.2015.07.035
18. Nieminen JO, Koponen LM, Ilmoniemi RJ (2015) Experimental characterization of the electric field distribution induced by TMS devices. Brain Stimul 8:582–589. https://doi.org/10.1016/j.brs.2015.01.004
19. Janssen A, Rampersad SM, Lucka F, Lanfer B, Lew S, Aydin U, Wolters CH, Stegeman F, Oostendorp TF (2013) The influence of sulcus width on simulated electric fields induced by transcranial magnetic stimulation. Phys Med Biol 58:4881–4896. https://doi.org/10.1088/0031-9155/58/14/4881
20. Porzig K, Brauer H, Toepfer H (2014) The electric field induced by transcranial magnetic stimulation: a comparison between analytic and fem solutions. Serbian J Electrical Eng 11:403–418. https://doi.org/10.2298/SJEE140908029P
21. Laakso I, Hirata A, Ugawa Y (2014) Effects of coil orientation on the electric field induced by TMS over the hand motor area. Phys

Med Biol 59:203–218. https://doi.org/10.1088/0031-9155/59/1/203.0402594v3
22. Petrov PI, Mandija S, Sommer IE, Van Den Berg CA, Neggers SF (2017) How much detail is needed in modeling a transcranial magnetic stimulation figure-8 coil: Measurements and brain simulations. PLoS One 12. https://doi.org/10.1371/journal.pone.0178952
23. Salinas FS, Lancaster JL, Fox PT (2009) 3D modeling of the total electric field induced by transcranial magnetic stimulation using the boundary element method. Phys Med Biol 54:3631–3647. https://doi.org/10.1088/0031-9155/54/12/002
24. Kim DH, Loukaides N, Sykulski J, Georghiou G (2004) Numerical investigation of the electric field distribution induced in the brain by transcranial magnetic stimulation. IEE Proc Sci Meas Tech 151:479–483. https://doi.org/10.1049/ip-smt:20040861
25. Janssen AM, Oostendorp TF, Stegeman DF (2015) The coil orientation dependency of the electric field induced by TMS for m1 and other brain areas. J Neuroeng Rehabil 12. https://doi.org/10.1186/s12984-015-0036-2
26. Laakso I, De Santis V, Cruciani S, Campi T, Feliziani M (2017) Modelling of induced electric fields based on incompletely known magnetic fields. Phys Med Biol 62:6567–6578. https://doi.org/10.1088/1361-6560/aa77a6
27. Salvador R, Silva S, Basser PJ, MP C (2011) Determining which mechanisms lead to activation in the motor cortex: a modeling study of transcranial magnetic stimulation using realistic stimulus waveforms and sulcal geometry. Clin Neurophysiol 122:748–758. https://doi.org/10.1016/j.clinph.2010.09.022
28. Richter L, Neumann G, Oung S, Schweikard A, Trillenberg P (2013) Optimal coil orientation for transcranial magnetic stimulation. PLoS One 8. https://doi.org/10.1371/journal.pone.0060358
29. Smith JE, Peterchev AV (2018) Electric field measurement of two commercial active/sham coils for transcranial magnetic stimulation. J Neural Eng 15. https://doi.org/10.1088/1741-2552/aace89
30. de Boor C (1978) A practical guide to splines. Springer, New York
31. Gomez LJ, Dannhauer M, Koponen LM, Peterchev AV (2020) Conditions for numerically accurate TMS electric field simulation. Brain Stimul 13:157–166. https://doi.org/10.1016/j.brs.2019.09.015
32. Byrd RH, Hribar ME, Nocedal J (1999) An interior point algorithm for large-scale nonlinear programming. SIAM J Optim 9:877–900. https://doi.org/10.1137/S1052623497325107
33. Asada T, Baba Y, Nagaoka N, Ametani A, Mahseredjian J, Yamamoto K (2017) A study on basic characteristics of the proximity effect on conductors. IEEE Trans Power Deliv 32:1790–1799. https://doi.org/10.1109/TPWRD.2016.2590962

A. V. Mancino received a BSc degree in electronics engineering from Instituto Tecnologico de Buenos Aires (ITBA) in 2014, where he is currently a teaching assistant in Signals and Systems, and in Biomedical Signal Processing. He is a PhD fellow at the National Scientific and Technical Research Council (CONICET), with research interests in signal processing, preoperative planning, and surgical navigation systems.

F. E. Milano, PhD received a BSc degree in information systems engineering from Universidad Tecnologica Nacional (UTN) in 2008 and a PhD in engineering from Instituto Tecnologico de Buenos Aires (ITBA) in 2016. He is currently an adjunct teacher in Biomedical Image Processing at ITBA and a software engineering consultant for Boston Scientific Corporation, with research interests in image analysis, surgical navigation systems and surgical tools tracking.

F. Martin Bertuzzi, MD Neurologist Staff at Neuromodulation Unit at Neurology Department, Hospital Italiano de Buenos Aires.

C. G. Yampolsky, MD Neurosurgeon, is currently Chairman of the Department of Neurosurgery, Hospital Italiano, Buenos Aires, Argentina and President of the Latin American Federation of Neurosurgical Societies (FLANC).

L. E. Ritacco, MD, PhD is the Coordinator of the Computer Assisted Surgery Unit, National Scientific and Technical Research Council (CONICET) - Instituto Universitario del Hospital Italiano (IUHI) - Hospital Italiano de Buenos Aires (HIBA), and Professor of Biomedical Engineering, IUHI, Buenos Aires, Argentina.

M. R. Risk, PhD, ScD, MBA is the Director of the Institute of Traslational Medicine and Biomedical Engineering (IMTIB), National Scientific and Technical Research Council (CONICET) - Instituto Universitario del Hospital Italiano (IUHI) - Hospital Italiano de Buenos Aires (HIBA), and Dean of Biomedical Engineering, IUHI, Buenos Aires, Argentina.